CHEMISTRY
A EUROPEAN JOURNAL

DOI: 10.1002/chem.200801814

Environmentally Friendly γ-MnO_2 Hexagon-Based Nanoarchitectures: Structural Understanding and Their Energy-Saving Applications

Changzheng Wu,[a] Wei Xie,[b] Miao Zhang,[a] Liangfei Bai,[a] Jinlong Yang,[a] and Yi Xie*[a]

Abstract: Although about 200,000 metric tons of γ-MnO_2 are used annually worldwide for industrial applications, the γ-MnO_2 structure is still known to possess a highly ambiguous crystal lattice. To better understand the γ-MnO_2 atomic structure, hexagon-based nanoarchitectures were successfully synthesized and used to elucidate its internal structure for the present work. The structural analysis results, obtained from the hexagon-based nanoarchitectures, clearly show the coexistence of akhtenskite (ε-MnO_2), pyrolusite (β-MnO_2), and ramsdellite in the so-called γ-MnO_2 phase and verified the heterogeneous phase assembly of the γ-MnO_2 state, which violates the well-known "De Wolff" model and derivative models, but partially accords with Heuer's results. Furthermore, heterogeneous γ-MnO_2 assembly was found to be a metastable structure under hydrothermal conditions, and the individual components of the heterogeneous γ-MnO_2 system have structural similarities and a high lattice matches with pyrolusite (β-MnO_2). The as-obtained γ-MnO_2 nanoarchitectures are nontoxic and environmentally friendly, and the application of such nanoarchitectures as support matrices successfully mitigates the common problems for phase-change materials of inorganic salts, such as phase separation and supercooling-effects, thereby showing prospect in energy-saving applications in future "smart-house" systems.

Keywords: environmental chemistry · manganese oxide · nanostructures · structure elucidation · X-ray diffraction

Introduction

About 200000 metric tons of γ-MnO_2 are used annually worldwide for industrial applications, and significant efforts are expended in a continual attempt to optimize and improve the material.[1] Despite the significant importance of γ-phase MnO_2, it possesses a highly disordered structure and an undefined, inexact crystal lattice.[2] Various structural models have been put forward to elucidate the internal structure of γ-MnO_2 by the refinement of its X-ray powder diffraction (XRD) data. De Wolff proposed that γ-MnO_2 is a random intergrowth of the pyrolusite and ramsdellite structures.[3] To better explain the characteristically broad and diffuse diffraction peaks in γ-MnO_2, Chabre and Pannetier introduced the additional concept of microtwinning in describing the γ-MnO_2 structure.[4] Later, Anderson et al. incorporated akhtenskite (ε-MnO_2) as one of the possible phases in γ-MnO_2, and their model describes γ-MnO_2 as a binary mixture of ε-MnO_2 and pyrolusite–ramsdellite intergrowth crystallites with different crystalline domain sizes.[5] Heuer et al. described γ-MnO_2 as a heterogeneous phase system that includes ≈30% ε-MnO_2, 15% β-MnO_2, and ≈50% ramsdellite.[2] The key reason for these various structural models of the γ-MnO_2 internal structure lies in the poor quality of XRD patterns obtained from most of γ-MnO_2 samples, in which broad peaks and high background noise caused γ-MnO_2 to be poorly characterized by XRD techniques. Due to the lack of efficient characterization methods that can give direct evidence for the structure of γ-MnO_2, the understanding of its structural model is still rather ambiguous. In this regard, electron diffraction (ED) and high-resolution transmission electron microscopy (HRTEM) may provide an alternative but more effective way to obtain direct evidence for the γ-MnO_2 structure. The advantages of ED and HRTEM over XRD arises from

[a] Dr. C. Wu, M. Zhang, L. Bai, Prof. J. Yang, Prof. Y. Xie
Hefei National Laboratory for Physical Sciences at Microscale
University of Science & Technology of China
Hefei, Anhui 230026, (P.R. China)
Fax: (+86) 551-3603987
E-mail: yxie@ustc.edu.cn

[b] Dr. W. Xie
Jonsson Comprehensive Cancer Center
University of California, Los Angeles, CA 90024 (USA)

Supporting information for this article is available on the WWW under http://dx.doi.org/10.1002/chem.200801814.

higher energy electrons and stronger atomic scattering,[6] allowing more of the two dimensional distribution of reciprocal lattice points to be revealed. Furthermore, ED can be combined with direct imaging of the sample, that is, high-resolution imaging of the crystal lattice, giving more direct evidence of the structure. Naturally, careful sample preparation will be important for the direct structural characterization. The sample to be studied must be electron transparent, meaning the sample thickness must be of the order of 100 nm or less; also, the selected area for ED and HRTEM should be representative of the structural characteristics of the whole sample. In this case, for γ-MnO_2, its mineral samples (nsutite) were not appropriate for such characterization.[7] Of course, a well-designed nanostructure with appropriate thickness and uniform morphology may provide an alternative opportunity to directly probe the internal crystal structure of γ-MnO_2 by ED and HRTEM. Herein, we introduce the large-scale hexagon-based nanoarchitectures of "layer-cake-like" and "intertexture-like" nanoarchitectures to the structural analysis of γ-MnO_2.

It is known that due to the highly anisotropic crystal lattice, the crystal can spontaneously form regular morphologies under the appropriate reaction conditions, in which the as-formed morphologies are actually the outward embodiment of the highly anisotropic internal structure.[8] As for γ-MnO_2, previously the fibrous morphology has been predominantly formed as nanowires,[9] well-aligned monocrystalline nanowires,[10] nanowire 3D nanostructures,[11] nanorod 3D urchins,[12] and so forth. Among the reported fibrous nanostructures, their growth direction was usually along the *c* axis, which is regarded as the chain growth direction for MnO_6 octahedra in γ-MnO_2. In this regard, the appearance of one-dimensional nanostructures is certainly not contradictory to the De Wolff model for γ-MnO_2, because the intergrowth of pyrolusite and ramsdellite structures has a chain like structure along the *c* axis. However, Zhu et al.[13] have reported the presence of hexagonal symmetry in the selected area electron diffraction (SAED) pattern of γ-MnO_2 irregular nanosheets and γ-MnO_2 hexagonal nanosheets, assembled in the form of nanospheres, have been reported by Suib et al.[14] Notably, despite different opinions on the γ-MnO_2 structure, the De Wolff model is still the most accepted model,[15] although the presence of hexagonal symmetry in γ-MnO_2 evidently violates the De Wolff model, since it is impossible to exhibit sixfold symmetry from the tetragonal pyrolusite, orthorhombic ramsdellite, or their intergrowth structures (see Supporting Information). In this regard, the appearance of a hexad axis in γ-MnO_2 products inspires us to further probe its internal structure. Of note, among all the known MnO_2 phases, only ε-MnO_2, known as the mineral akhtenskite, definitely possesses hexagonal symmetry in its atomic crystal lattice.[16] In ε-MnO_2, the single and double MnO_6 octahedral chains running parallel to the *c* axis undergo many changes of direction at 60/120° upon twinning to form a hexagonal NiAs-type unit cell with the space group *P*63/*mmc*.[17] Then the question arises from the appearance of hexagonal symmetry in γ-MnO_2 samples: would ε-MnO_2 as a component in the heterogeneous phase γ-MnO_2 explain the hexagonal symmetry structure? Or is γ-MnO_2 actually a hexagonal phase? To answer such questions, further development of γ-MnO_2 nanostructures with high purity and well-defined morphology is certainly an intriguing method.

The γ-MnO_2 hexagon-based nanoarchitectures, including "layer-cake-like" and "intertexture-like" structures, could be obtained by a simple hydrothermal reaction of $MnSO_4$ and $NaBrO_3$ at 120 °C. The "intertexture-like" nanoarchitectures evolved from the "layer-cake-like" structures by elongating the reaction time and by implementing the "solid–solution–solid" growth mechanism. The presence of hexagonal symmetry in the synthesized γ-MnO_2 hexagon-based nanoarchitectures violates the known pyrolusite–ramsdellite intergrowth model for γ-MnO_2. Due to the small size and morphology uniformity of the grown nanorods, the "intertexture-like" nanoarchitectures give us an alternative way to further investigate the internal structural details of γ-MnO_2. Also, it was found that the "intertexture like" nanoarchitectures are nontoxic and environmentally friendly, and as such might be used in energy-saving applications in future "smart-house" systems.

Results and Discussion

The characterization of γ-MnO_2 "layer-cake-like" nanoarchitectures: The phase and chemical composition information for the as-obtained product treated at 120 °C for 2 h is revealed by the X-ray powder diffraction (XRD) and X-ray photoelectron spectroscopy (XPS) data. The XRD pattern is shown in Figure 1a and provides structural information. All of the reflection peaks can be readily indexed to the well-known "γ-MnO_2" (JCPDS card 14–644, $a=6.36$ Å, $b=10.15$ Å, $c=4.09$ Å), which already appeared in recent reports for γ-MnO_2,[10–12,18], further confirming the as-obtained product is indeed the γ-MnO_2. The XPS survey spectrum (Figure 1b) reveals that the as-obtained sample consists of the elements Mn and O, while no evident impurities, for example, sodium ions or elemental sulfur, are detected. The Mn 2p core level spectrum (inset in Figure 1b) illustrates that the observed values of the binding energies for Mn 2p3/2 and Mn 2p1/2 (641.65 and 653.60 eV, respectively) are in agreement with the literature values for bulk Mn^{4+}.[19] All these results indicate that the sample is γ-MnO_2, and the XPS spectra show no evident impurities detected in the samples (resolution limit: 1 at.%).

The hexagonal symmetry nanostructures for γ-MnO_2, synthesized by the reaction of $MnSO_4$ and $NaBrO_3$ at 120 °C for 2 h, were present on a large scale as observed in the FE-SEM images. Figure 2a shows a typical panoramic FE-SEM image of the γ-MnO_2 product. The magnified SEM image (Figure 2b) exhibits the dominant morphology of hexagonal "layercake-like" nanoarchitectures with an edge length ranging from about 800 nm to 2 μm. Each "layer cake" exhibits well-defined hexagonal geometry with six symmetrical edges and is composed of clearly distinguished platelet-like

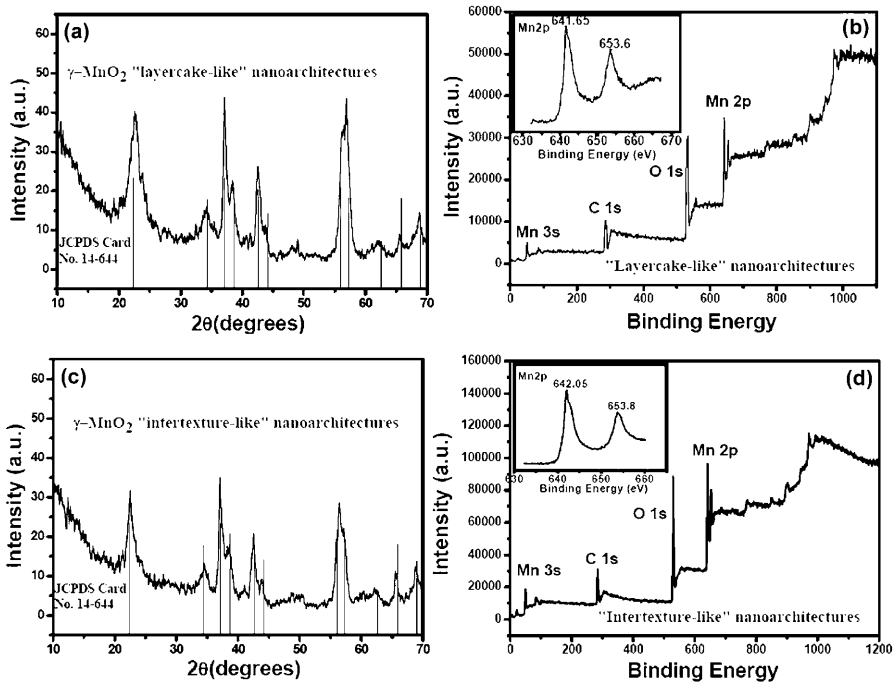

Figure 1. XRD patterns (a and c) and XPS survey spectra (b and d) of as-obtained γ-MnO_2 "layer-cake-like" and "intertexture-like" nanoarchitectures, respectively. From the XRD patterns and XPS spectra, the as-obtained hexagon-based nanoarchitectures are identified as the so-called "γ-MnO_2".

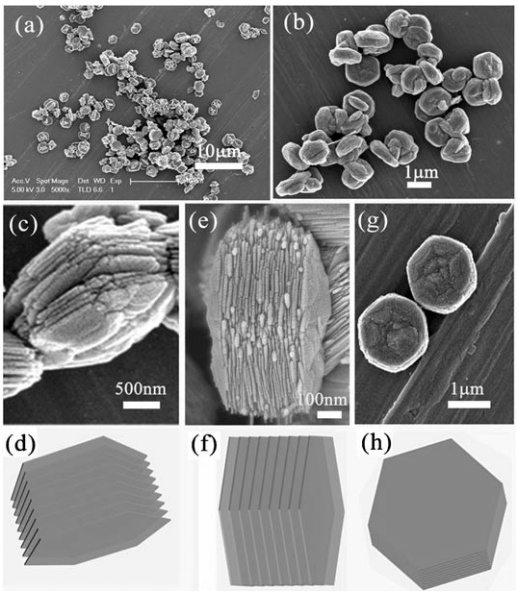

Figure 2. The FE-SEM images (a,b) of the γ-MnO_2 product obtained by the direct reaction of $MnSO_4$ and $NaBrO_3$ at 120 °C, in which the hexagonal symmetry nanoarchitectures are clearly seen. Typical "layer-cake-like" nanoarchitectures with different orientations are shown in c), e), and g), and their nanoarchitectures are schematically expressed with the stacked hexagonal plates as shown in d), f), and h), respectively.

layers. Close views show that the nanoarchitectures form an ordered arrangement through the layer-by-layer stacking of hexagonal sheets. To better explain how the "layer-cake-like" nanoarchitectures with different orientations are assembled by the platelet like layers, the nanoarchitectures as shown in Figure 2c, e and g are schematically illustrated in Figure 2d, f and h, respectively.

Moreover, the HRTEM images and ED pattern (Figure 3) on the edge of hexagonal "layer-cake-like" nanoarchitectures also show the presence of hexagonal symmetry in the as-obtained products. The ED pattern (Figure 3b) of the margin of a typical "layer cake" exhibits hexagonal symmetry, confirming the existence of hexagonal symmetry in the γ-MnO_2 product.

The contradiction between the existing crystallographic hexagonal symmetry in the sample and the pyrolusite–ramsdellite intergrowth model for γ-MnO_2: The as-obtained γ-MnO_2 nanoarchitectures exhibit a well-defined hexagonal geometry with six-symmetrical edges, and the corresponding selected area electron diffraction (SAED) data of the "layer cake" also show the hexagonal symmetric spots. In this case, the SAED results seem consistent with the macroscopic morphological symmetry. However, the presence of hexagonal symmetry in the γ-MnO_2 product evidently violates the De Wolff model, which described γ-MnO_2 as an irregular intergrowth of ramsdellite and pyrolusite, because it is impossible for the pyrolusite, ramsdellite, or their intergrowth structure to exhibit hexagonal symmetry (see Supporting Information).

It should be noted that the De Wolff model for γ-MnO_2 has been known for more than 50 years and is still widely used to describe the γ-MnO_2 crystal structure.[7,10–12,18] The pyrolusite and ramsdellite structures have similar arrangements along the *a* and *c* axes and infinite strings of MnO_6 octahedra can only grow along the *b* axis. Furthermore, a comprehensive description of γ-MnO_2 has also been pro-

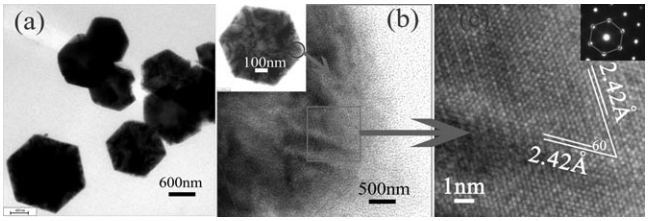

Figure 3. a) and b): HRTEM images and ED patterns of the corners of typical "layer-cake-like" nanoarchitectures.

posed based on two kinds of defects, intergrowths and twinning, within the ramsdellite structure.[20] These results reveal that the γ-MnO_2 has two components, pyrolusite and ramsdellite. As for the pyrolusite (β-MnO_2), single chains of edge-sharing $Mn^{IV}O_6$ octahedra share corners with neighboring chains to form a framework structure containing tunnels with square cross-sections with one octahedron on each side of the square.[21] For the ramsdellite MnO_2, the $Mn^{IV}O_6$ octahedra are linked in double chains, each consisting of two adjacent single chains that share octahedral edges; the double chains, in turn, link corners with each other to form a framework with tunnels that have a rectangular-shaped cross-section with 1×2 octahedra on a side.[22] For these two concerned structures, pyrolusite has a tetragonal system with the space group $P4_2/mnm$ and ramsdellite has an orthorhombic system in the *Pnam* space group, neither of which can exhibit hexagonal symmetry based on their space groups. Therefore, a contradiction occurs between the current hexagonal symmetry in the sample and the classical De Wolff model based on pyrolusite–ramsdellite intergrowth. However, among all the known MnO_2 phases, only ε-MnO_2 definitely possesses the hexagonal symmetry in its atomic crystal lattice, in which the structure of akhtenskite (ε-MnO_2) consists of single and double MnO_6 octahedral chains that run parallel to the *c* axis and undergo many changes of direction at 60/120° upon twinning to form a hexagonal NiAs-type unit cell with the space group *P*63/*mmc*.[16–17] Therefore, the questions arise once again: does the appearance of hexagonal symmetry in γ-MnO_2 originate from the presence of ε-MnO_2 as a component in γ-MnO_2 or does the whole γ-MnO_2 possess the hexagonal-symmetry structure?

Further investigations into the structure of "intertexture-like" γ-MnO_2 nanoarchitectures: Although the hexagonal "layer-cake-like" nanoarchitectures were the dominant morphology in Figures 2 and 3 and the corresponding hexagonal-symmetry ED pattern could also be observed in the γ-MnO_2 sample, it is still necessary to further investigate the structural details, owing to the presence of many defects in these nanoarchitectures. Also, the "layer cakes" were so thick that the electron beam of the HRTEM was not able to transmit through the sample to achieve reliable ED patterns and HRTEM images, adding to the difficulty of clearly understanding the structural details for the whole γ-MnO_2.

Our experiments find that the one-dimensional nanostructures of nanorods could be grown radially from the hexagonal center by elongating their reaction time (see Supporting Information), forming the "intertexture-like" nanoarchitectures (Figure 4). The XRD pattern (Figure 1c) for these nanoarchitectures reveals that the product is still in the γ-MnO_2 form. The XPS spectra (Figure 1d) further indicate that the as-obtained product has the Mn/O molar ratio of 1:2.01 and no other impurities can be found (see Supporting Information). Figure 4 shows that all of the samples are uniform "intertexture-like" nanoarchitectures with the diameter of 1–8 μm, and the proportion of the "intertexture-like"

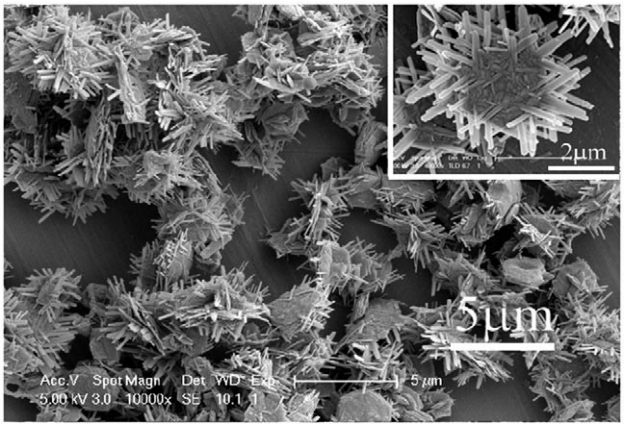

Figure 4. The FESEM image of "intertexture-like" nanoarchitectures.

nanoarchitectures in the whole sample is above 95%. Careful observation (inset in Figure 4) found that these nanoarchitectures consist of the nanorods with a diameter of 80–200 nm and a length up to about 1 μm, and all of the nanorods grew radially from the edges of hexagonal core particles.

Due to the small size and morphology uniformity of the grown nanorods, the "intertexture-like" nanoarchitectures give us an alternative way to further investigate the structural details of the γ-MnO_2 product. These nanorods are thin enough to be easily transmitted by the electron beam from TEM to achieve reliable ED patterns and HRTEM images during the structural characterization process. Firstly, the pyrolusite (β-MnO_2) was detected based on the careful analysis of HRTEM and SAED results. The inset in Figure 5a shows a representative SAED pattern taken from a typical nanorod that was grown from a hexagonal core particle and

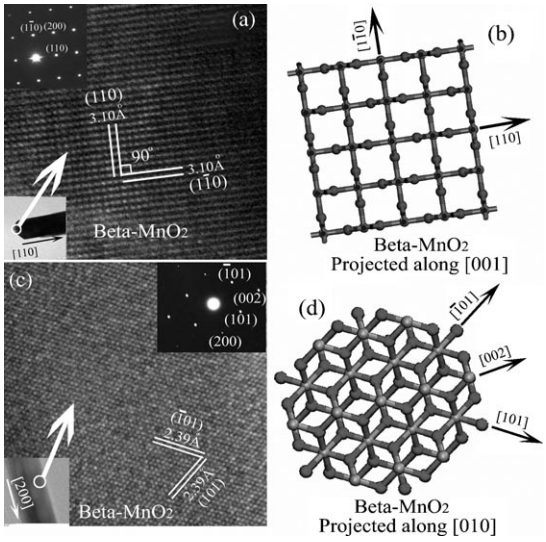

Figure 5. a) and c): HRTEM images and SAED patterns taken from two individual nanorods, in the "intertexture-like" nanoarchitectures. b) and d): The corresponding atomic models for the HRTEM images in a) and c), respectively.

can be indexed to the reflection of the tetragonal β-MnO_2 [001] axis. The lattice fringes in Figure 5a show two sets of perpendicularly lattice spacing of about 3.10 Å that correspond to the (110) and (1$\bar{1}$0) planes of β-MnO_2. It should be noted that the HRTEM image and SAED pattern along the [001] axis have been experimentally determined in the previous reports,[23] confirming the existence of pyrolusite (β-MnO_2) in the sample. Our experimental ED pattern shown in Figure 5a gives the same symmetrical dotted lattice and lattice fringes. Also, the atomic model of β-MnO_2 projected along the [001] axis exhibits tetragonal symmetry. The [110] and [1$\bar{1}$0] axes are indicated by the arrows in Figure 5b, giving further evidence for the existence of β-MnO_2. Moreover, the SAED pattern and HRTEM image (Figure 5c) taken from another nanorod confirms the presence of β-MnO_2. The two interplanar spaces of about 2.39 Å with the angle value of 66.3° correspond to the (101) and ($\bar{1}$01) plane of tetragonal β-MnO_2. The SAED pattern in the inset in Figure 5c reveals the single-crystalline nature, and can be indexed to the [010] axis of tetragonal β-MnO_2. The atomically crystal structure projected along [010] is shown in Figure 5d gives the same symmetry as in the SAED pattern, confirming the indexing of this SAED pattern to β-MnO_2 and providing more diagnostic and direct evidence for the existence of the pyrolusite phase in γ-MnO_2.

In addition, as shown in Figure 6a, both HRTEM image and its ED pattern give the information that the selected nanorod contains ramsdellite MnO_2 according to the

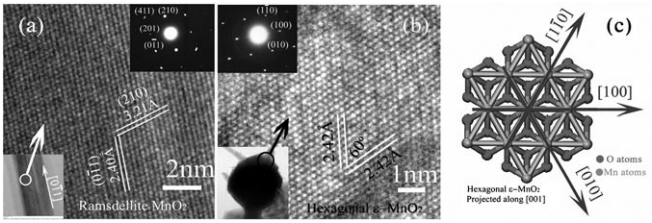

Figure 6. a) and b): HRTEM images and SAED patterns taken from one typical nanorod and the marginal area of hexagonal core in the "intertexture-like" nanoarchitectures. c) The corresponding atomic model for the HRTEM image shown in b).

interplanar spacing distances and the angle values of each crystal planes. The interplanar distances of 2.40 and 3.21 Å match well with the $d_{0\bar{1}1}$ and d_{210} spacing of ramsdellite MnO_2, respectively, indicating that the nanorod was growing along [0$\bar{1}$1] direction. Also, all the orientation angle values of these planes appeared in the SAED patterns, such as (0$\bar{1}$0), (201), (210), and (411), and are fairly consistent with those calculated from orthorhombic crystallographic parameters of ramsdellite MnO_2, providing the further solid evidence for the existence of the ramsdellite form in the nanorod of as-obtained γ-MnO_2 sample (see Supporting Information). Of note, other crystallographic forms for MnO_2 were also studied with respect to fitting the crystallographic parameters from the ED pattern and HRTEM image as shown in Figure 6a, but the crystallographic calculation did not lead to improved results and their theoretical angle values did not agree with the experimental results.

Hexagonal ε-MnO_2 was also found at the typical margin of hexagonal core particle. Since the presence of the ramsdellite phase in the γ-MnO_2 sample makes it impossible to assign the obtained so-called "γ-MnO_2" to a hexagonal phase, and only ε-MnO_2 possesses the hexagonal symmetry among all of the MnO_2 crystallographic forms, then the hexagonal symmetry dots in the SAED provide the evidence for the presence of ε-MnO_2 in this case. The interlayer spacing in Figure 6b is about 2.42 Å, which is consistent with the *d* value of the (100) crystal plane of ε-MnO_2 (JCPDS card 30-0820), from which it can be deduced that the HRTEM images were obtained from the projection direction of [001]. The atomic model of ε-MnO_2 in Figure 6c also supports the hexagonal symmetry in ε-MnO_2, showing good matching for the symmetry and the atomic arrangements of ε-MnO_2 in the "γ-MnO_2" sample.

Briefly, the combined analysis of the SAED pattern and the HRTEM images indicates that the "intertexture-like" nanoarchitectures of γ-MnO_2 contain three phases, akhtenskite (ε-MnO_2), pyrolusite (β-MnO_2), and ramsdellite. That is to say, γ-MnO_2 is a heterogeneous phase system, which violates the De Wolff model and its derivative models for γ-MnO_2, but partially confirms Heuer's results.[2] In addition, the conclusion of heterogeneous phase assembly of γ-MnO_2 is consistent with the XRD refinement results, in which the XRD pattern of "γ-MnO_2" also could be known as the three-phase XRD fitting of akhtenskite (ε-MnO_2), pyrolusite (β-MnO_2), and ramsdellite.[4–5] Furthermore, the three phases in "γ-MnO_2" are independently located at different positions in the "intertexture-like" nanoarchitectures, and the hexagonal-symmetry structure only lies in the hexagonal core particles and cannot be found in any of the nanorods. The hexagon-based morphology of ε-MnO_2 is in fact the outward embodiment of its hexagonal internal structure. Meanwhile, the pyrolusite (β-MnO_2) and ramsdellite are only found in the nanorods, but not the hexagonal core particles; the growth morphology of the one-dimensional nanorods actually embodies the linear MnO_6 octahedral chains in the internal crystal lattice of β-MnO_2 and ramsdellite.[10,23] From the viewpoint of macroscopic morphology characteristics, the morphologies in the γ-MnO_2 sample were usually the outward embodiment of the internal crystal lattices of its phase components, providing an alternative clue as to the morphology of the γ-MnO_2 structure.

The state transformation from heterogeneous "γ-MnO_2" to β-MnO_2: As described above, the known γ-MnO_2 is in fact the heterogeneous phase system made up of akhtenskite (ε-MnO_2), pyrolusite (β-MnO_2), and ramsdellite. Moreover, our comparable experiments find that the heterogeneous γ-MnO_2 only transforms into one of its components: β-MnO_2, which is the most stable structure among all the phase components of γ-MnO_2.

Systematic experiments were carried out to investigate the reaction parameters that are required for the γ-phase

formation and its transformation from γ-MnO_2 to β-MnO_2. At the relatively low reaction temperature of 120 °C, the squares in Figure 7a represent γ-MnO_2 and fill the entire

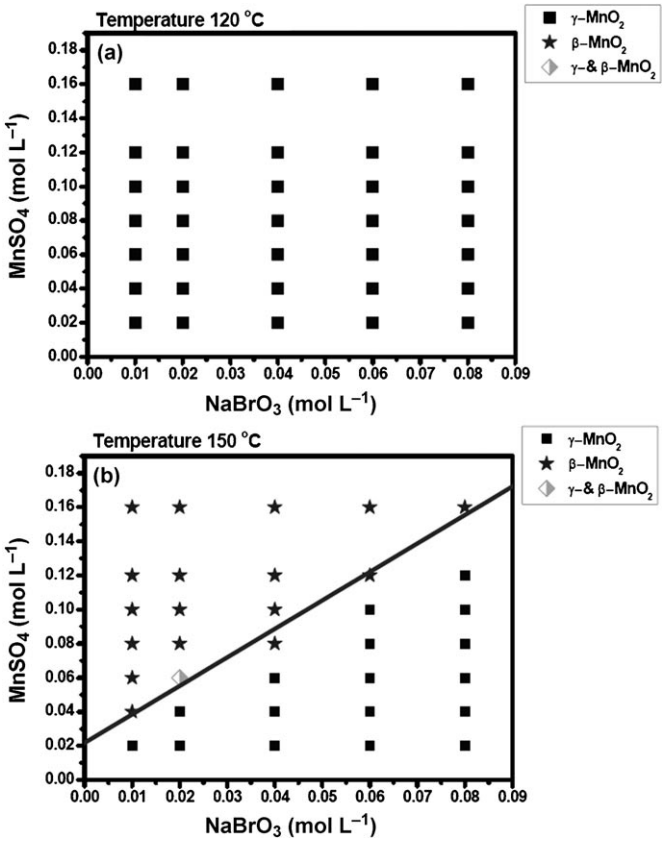

Figure 7. The state transformation between γ- and β-MnO_2 with the evolution of $[Mn^{2+}]$ and $[BrO_3^-]$ at the reaction temperature of 120 °C (a) and 150 °C (b).

concentration range of BrO_3^- and Mn^{2+}, showing that only γ-MnO_2 forms under these conditions. That is, γ-MnO_2 is stable and easily formed at the relatively low temperatures in the concentration range of 0.01–0.09 mol L^{-1} for BrO_3^- and 0.02–0.16 mol L^{-1} for Mn^{2+}. At the elevated reaction temperature of 150 °C, there is a state transformation from γ-MnO_2 to β-MnO_2, as shown in Figure 7b, in which the points under the line can be assigned to γ-MnO_2 and β-MnO_2 is distributed above the line. The equation corresponding to this line [Eq. (1)] can be found by linearly fitting the selected points adjacent to the γ-MnO_2 area.

$$[Mn^{2+}] = 0.022+1.67 \cdot [BrO_3^-] \quad (1)$$

It can be seen that the high concentration of $[Mn^{2+}]$ plays a more crucial role than that of $[BrO_3^-]$ for the formation of β-MnO_2 in the reaction systems. In detail, a high concentration of $[Mn^{2+}]$ usually leads to the formation of β-MnO_2 keeping other reaction parameters constant. For example, when the $[BrO_3^-]$ concentration is 0.01 mol L^{-1} during the reaction process, a low $[Mn^{2+}]$ concentration of 0.02 mol L^{-1} gives the γ-MnO_2, while a higher concentration, above 0.04 mol L^{-1}, leads to the formation of the β-phase MnO_2. Similar cases can also be found in the case of other $[BrO_3^-]$ concentration systems, confirming that higher $[Mn^{2+}]$ concentrations favor the formation of β-MnO_2. In contrast, increasing the $[BrO_3^-]$ concentration did not favor the formation of β-MnO_2 when a low concentration of $[Mn^{2+}]$ is used. For example, at the $[Mn^{2+}]$ concentration of 0.06 mol L^{-1}, the higher $[BrO_3^-]$ concentration above 0.02 mol L^{-1} resulted in the γ-MnO_2, suggesting that a higher concentration of BrO_3^- is a disadvantage for β-MnO_2 formation. According to the Gibbs free-energy formula [Eq. (2)], an increased concentration of the reactants can lead to the formation of more stable final products.

$$\Delta_r G_m^\theta = RT \cdot \ln\left(\frac{[Mn^{2+}]^5[BrO_3^-]^2}{[H^+]^8}\right) \quad (2)$$

In Equation (2) $\Delta_r G_m^\theta$ is the Gibbs free energy, $R = 8.314\ J\,K^{-1}\,mol^{-1}$, and T is absolute temperature.

Therefore, the energy barrier theory from the Gibbs free-energy formula cannot be applied to explain the state transformations from γ-MnO_2 to β-MnO_2 in the present reaction systems. However, high concentrations of $[Mn^{2+}]$ has more advantages for the formation of β-MnO_2, which is certainly related especially to the structural characteristics of the three phases in γ-MnO_2. As for the γ-MnO_2 heterogeneous phase assembly, the akhtenskite (ε-MnO_2), pyrolusite (β-MnO_2), and ramsdellite all consist of a hexagonal close packed lattice of oxygen ions with Mn^{2+} cations occupying half of the octahedral sites. In this regard, the different arrangements of Mn atoms in such an oxygen framework determine the phase of MnO_2.[24] To better elucidate this, a schematic representation of akhtenskite (ε-MnO_2), pyrolusite (β-MnO_2), and ramsdellite showing the occupied Mn atoms (represented by filled cycles) and vacant octahedral sites (represented by empty sites) is given in Figure 8. Due to such atomic configurations for MnO_2, it is understandable that the higher Mn^{2+} ion concentration added the possibility to form the most stable configuration, that is, the pyrolusite.[20] Also, first-principle calculations performed with the VASP program were undertaken to get the exact energy of the three kinds of MnO_2 (ε-MnO_2, β-MnO_2, and ramsdellite). The results revealed that pyrolusite (β-MnO_2) has the lowest energy when compared with ε-MnO_2 and ramsdellite as shown in Table 1. Therefore, a high concentration of Mn^{2+} could easily give the optimized arrangement with the lowest energy, achieving the stable β-MnO_2 phase when a relatively high temperature is provided. To summarize, γ-MnO_2 is a metastable, heterogeneous phase composed of akhtenskite (ε-MnO_2), pyrolusite (β-MnO_2), and ramsdellite, and the ramsdellite and ε-MnO_2 components in "γ-MnO_2" can transform to the more stable pyrolusite (β-MnO_2) under high Mn^{2+} concentrations. This shows that all of the components in "γ-MnO_2" have structural similarities and low lattice mismatches with pyrolusite (β-MnO_2) and provide an al-

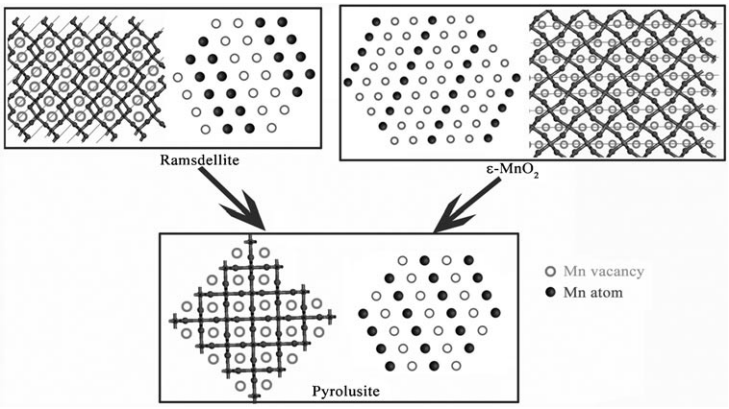

Figure 8. Schematic representation of the structure of ramsdellite and pyrolusite, and the lattice gas representation of the Mn^{2+} ion lattice for a) ramsdellite, b) ε-MnO_2, and c) pyrolusite, showing the basal plane of the hexagonal close packed structure. Only Mn atoms (represented by filled circles) and vacant octahedral site (represented by empty circles) are presented.

Table 1. The atomic total energy for three kinds of MnO_2 structures: akhtenskite, pyrolusite, and ramsdellite, according to the first-principle calculation by the VASP program.

Structure	Chemical formula	E_{total} [eV]
pyrolusite	β-MnO_2	-92.70
ramsdellite	R-MnO_2	-91.82
akhtenskite	ε-MnO_2	-91.56

ternative way to understand the structural information of γ-MnO_2.

The biosafety of γ-MnO_2 "intertexture-like" nanoarchitectures: To test the biosafety of the MnO_2 "intertexture-like" nanoarchitectures, we tested the viability of different human cell lines after treatment of MnO_2 "intertexture-like" nanoarchitectures by an MTT (MTT = methylthiazolyldiphenyltetrazolium bromide) assay (see Experimental Section for details), in which yellow MTT is added to cells and reduced to purple formazan in the mitochondria of living cells; thus the concentration of formazan produced directly reflects the number of viable cells. The cells were treated with 0–200 $\mu g\,mL^{-1}$ of MnO_2 "intertexture-like" nanoarchitectures for 24 h and then applied to the MTT assay. To demonstrate the generalization of our experiments, three human cell lines, derived from different tissues, were included in this assay. As shown in Figure 9a,b, when compared with the pure cells without any treatments, the cells treated with MnO_2 "intertexture-like" nanoarchitectures did not show any apparent loss of viability. The cells are quite healthy and did not show any viability loss when treated with different concentrations of MnO_2 "intertexture-like" nanoarchitectures and kept for 24 h (Figure 9a). Only when the concentration was increased to 200 $\mu g\,mL^{-1}$, which is a very high concentration when compared to previous experiments[25] (Figure 9b), was a slight decrease in viability noticeable. Moreover, we also treated cells for different lengths of time to examine if the cell viability would be impaired when cells were exposed to MnO_2 "intertexture-like" nanoarchitectures for longer times. When we treated the cells with 50 $\mu g\,mL^{-1}$ of MnO_2 "intertexture-like" nanoarchitectures (Figure 9c), cell growth seems to have been suppressed, but no apparent cell toxicity was observed even

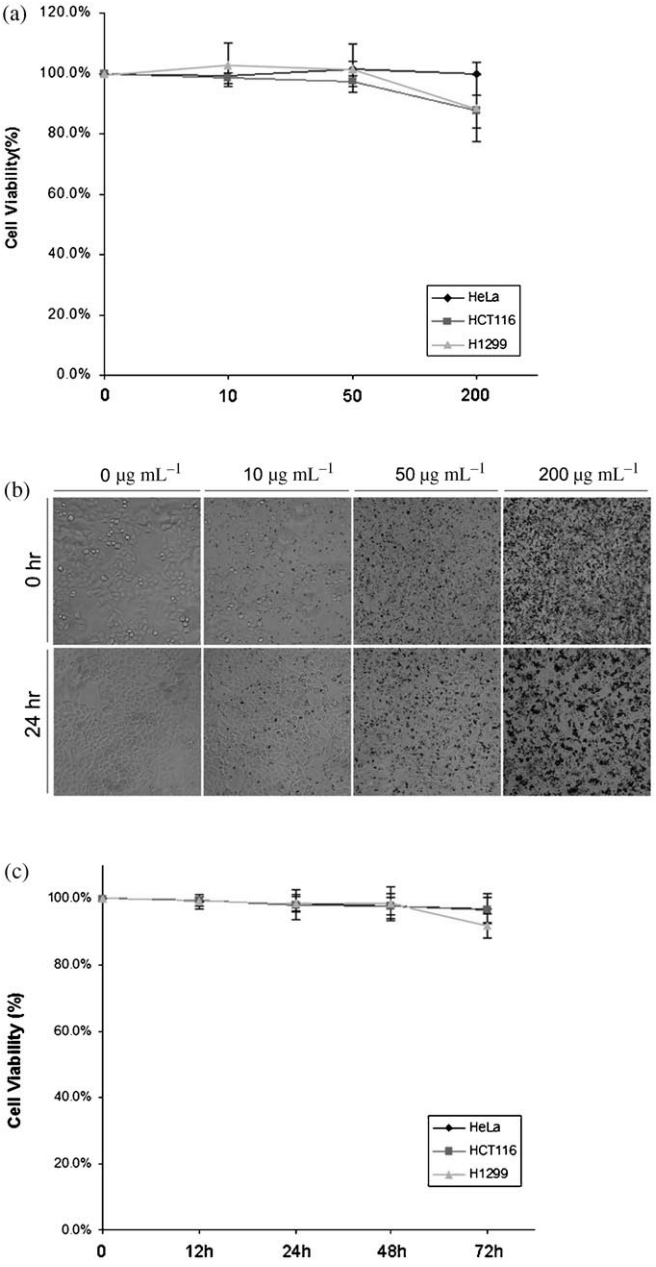

Figure 9. Cell viability after treatment of MnO_2 "intertexture-like" nanoarchitectures. a) Cells were treated with the indicated concentration of MnO_2 "intertexture-like" nanoarchitectures for 24 h and then applied to a MTT assay to measure cell viability as described in the experimental section. b) Pictures of cells treated as described in a). c) Cells treated with MnO_2 "intertexture-like" nanoarchitectures (50 $\mu M\,mL^{-1}$) for different lengths of time and then applied to MTT assays to measure cell viability. In a) and c) each data point represents the results from at least three independent experiments. Vertical error bars are the standard deviations from the mean of the values within three standard deviations.

after 72 h of treatment. Taken together, the heterogeneous phase γ-MnO_2 "intertexture-like" nanoarchitectures did not show evident cell toxicity and is an overall safe and environmentally friendly material.

Energy-saving applications of γ-MnO_2 "intertexture-like" nanoarchitectures: For most salt hydrates, especially those proposed for energy saving applications, their asymmetrical melting and freezing behavior usually decreases their potential as an energy-storing medium and also limits their usefulness for temperature calibration applications.[26] The application of environmentally friendly γ-MnO_2 "intertexture-like" nanoarchitectures as the supporting matrix led to performance advantages for the mitigation of supercooling effects and phase separation during the crystalline cooling process. As shown in Figure 10, although the endothermal peaks for

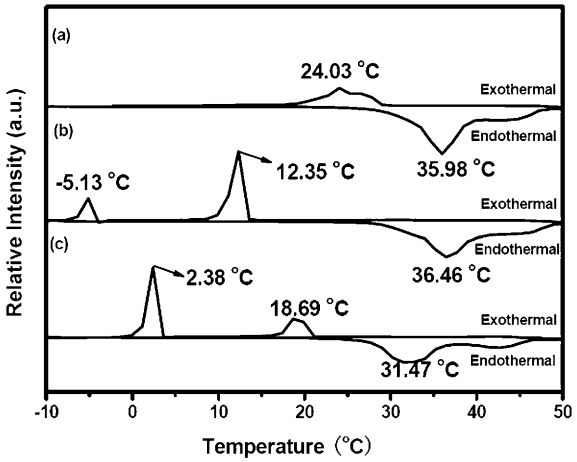

Figure 10. DSC thermal spectra of a) nanoarchitectured MnO_2/$CaCl_2$·6H_2O, b) commercial MnO_2/$CaCl_2$·6H_2O, and c) pure $CaCl_2$·6H_2O systems. Heat rate 5 K min^{-1}.

the MnO_2-participation system are slightly higher than those for pure $CaCl_2$·6H_2O in the endothermal curves, the nanoarchitectured MnO_2/$CaCl_2$·6H_2O system has more benefits than the commercial MnO_2/$CaCl_2$·6H_2O and pure $CaCl_2$·6H_2O systems. The exothermal curves for nanoarchitectured MnO_2/$CaCl_2$·6H_2O systems show only one peak centered at 24.03 °C in the exothermal curve (Figure 10a), while dual sets of peaks appeared for commercial MnO_2/$CaCl_2$·6H_2O (12.35 °C and −5.13 °C; Figure 10b) and pure $CaCl_2$·6H_2O (18.69 °C and 2.38 °C; Figure 10c) system. That is, the supercooling and phase separation phenomena in the nanoarchitectured MnO_2/$CaCl_2$·6H_2O system are inhibited when compared to the commercial MnO_2/$CaCl_2$·6H_2O and pure $CaCl_2$·6H_2O systems. Of note, the mitigation of the supercooling effect is due to the small size effect of the nanounits and the porous structure that comes from nanoarchitectures, which enables the MnO_2 to uniformly disperse in the melting $CaCl_2$·6H_2O during heating. In this case, heterogeneous nucleation[27] occurs during the crystallization process resulting in reducing the supercooling effect. However, the commercial MnO_2 has large diameter sizes and cannot be easily dispersed in the melting $CaCl_2$·6H_2O system during the heating process and is usually deposited in the container pan. In this case, the homogenous nucleation[28] of the phase change material of $CaCl_2$·6H_2O are responsible for the cooling crystallization process, and is similar to that for pure $CaCl_2$·6H_2O, and leads to the supercooling phenomena. Put concisely, the application of the nanoarchitectures as a supporting matrix for phase-change materials mitigates common problems, such as phase separation and supercooling effects, thereby showing potential application for energy-saving in future "smart-house" systems.

Conclusions

In summary, the γ-MnO_2 hexagon-based "layer-cake-like" and "intertexture-like" nanoarchitectures were successfully synthesized for the first time by a simple hydrothermal reaction of $MnSO_4$ and $NaBrO_3$. Based on direct evidence from the structural analysis of hexagon-based nanoarchitectures, the γ-MnO_2 state was found to consist of akhtenskite (ε-MnO_2), pyrolusite (β-MnO_2), and ramsdellite, forming a heterogeneous phase, which violates the "De Wolff" model and derivative models for γ-MnO_2, but it partially agrees with Heuer's results.[2] Furthermore, the heterogeneous γ-MnO_2 was found to be a metastable, hydrothermal structure, and the components of heterogeneous γ-MnO_2 have the structural similarity and high lattice matches to pyrolusite (β-MnO_2). The as-obtained γ-MnO_2 nanoarchitectures are nontoxic and environmentally friendly, and have potential application as support matrices, mitigating common problems for phasechange materials of inorganic salts such as phase separation and supercooling effects, and ultimate use in energy-saving applications in future "smart-house" systems.

Experimental Section

The chemical reaction we employed for the synthesis of the γ-MnO_2 nanoarchitectures can be formulated as Equation (3)

$$5\,MnSO_4 + 2\,NaBrO_3 + 4\,H_2O \rightarrow 5\,\gamma\text{-}MnO_2 + Br_2 + Na_2SO_4 + 4\,H_2SO_4 \quad (3)$$

To prepare γ-MnO_2 "layer-cake-like" nanoarchitectures, an aqueous solution (50 mL) containing of $MnSO_4$ (1 mmol) and of $NaBrO_3$ (0.5 mmol) was put in a conical flask, and was stirred with a magnetic stirrer until a transparent solution was obtained. The solution was then transferred into a 60 mL Teflon-lined stainless steel autoclave, sealed, and was slowly heated to 120 °C with a rate of 1 °C min^{-1}. The autoclave was maintained at 120 °C for 2 h. Only by elongating the reaction time to 16 h could γ-MnO_2 "intertexture-like" nanoarchitectures be obtained. Also, it should be noted that the comparable experiments were carried out by adjusting the experimental parameters with the other reaction conditions remaining constant. After the reaction was completed, the resulting black solid was filtered, washed with distilled water and absolute ethanol to remove byproducts, and then dried at 60 °C in air. The obtained black powders were collected for the following characterizations.

Characterization details: The sample was characterized by X-ray powder diffraction (XRD) with a Philips X'Pert Pro Super diffractometer with $Cu_{K\alpha}$ radiation ($\lambda = 1.54178$ Å). The field emission scanning electron microscopy (FE-SEM) images were taken on a JEOL JSM-6700F SEM. The transmission electron microscopy (TEM) images, electron diffraction (ED) patterns and high-resolution transmission electron microscopy (HRTEM) images were recorded on a JEOL-2010 TEM at an acceleration voltage of 200 KV. X-ray photoelectron spectroscopy (XPS) measurements were performed on a VGESCALAB MKII X-ray photoelectron spectrometer with an exciting source of $Mg_{K\alpha} = 1253.6$ eV.

Total energy calculations: The VASP[19] program, a periodic DFT program that uses the projector augmented wave (PAW) method,[20] was utilized. The geometric optimization process was carried out by using a convergence of 2 meV for VASP. For the VASP calculations, convergence was attained with an $8 \times 8 \times 8$ Monkhorst-Pack[21] k-point grid and plane wave and augmentation charge cutoffs of 780 and 400 eV.

Materials and methods for biosafety studies of γ-MnO_2 "intertexture like" nanoarchitectures

Cell cultures: Human cervical carcinoma cell line HeLa, Human non-small cell lung carcinoma cells (NSCLC) H1299 and Human colon carcinoma cell line HCT116 were grown in Dulbecco's modified Eagle's medium supplemented with 10% (V/V) fetal bovine serum (FBS), 1× nonessential amino acid (1 equiv),penicillin (100 $\mu g\,mL^{-1}$), sodium pyruvate (1 equiv), and streptomycin (100 $\mu g\,mL^{-}$). The culture medium was purchased from Invitrogen Corporation (GIBCO, Grand Island, NY). The cells were maintained at 37 °C in a humidified 5% CO_2-containing atmosphere.

MTT assay: Briefly, 10000 cells per well of each cell line were seeded in 96-well plate and treated with MnO_2 nanoparticles (0–200 $\mu g\,mL^{-1}$) suspended in culture medium for the appropriate periods of time. Freshly made MTT (Sigma–Aldrich) solution was added to the culture medium to reach a final concentration of 500 $\mu g\,mL^{-}$. The cells were put back into incubator. After an additional 4 h, the culture medium was poured off and DMSO (200 μL; Sigma–Aldrich) was added into each well. After complete dissolution of blue crystals, a microplate reader was used to measure the absorption at 570 nm.

Thermal energy-storage applications: The samples for $MnO_2/CaCl_2{\cdot}6H_2O$ mixture systems were prepared from MnO_2 sample (20 mg) and $CaCl_2{\cdot}6H_2O$ (1.5 g) by vacuum ultrasonification for 30 min at 35 °C. After cooling to 0 °C, the sample was thoroughly mixed using an agate mortar in order to ensure uniform dispersion of the MnO_2 sample in the melting $CaCl_2{\cdot}6H_2O$. For differential scanning calorimeter (DSC) measurements, the samples of pure $CaCl_2{\cdot}6H_2O$ and $MnO_2/CaCl_2{\cdot}6H_2O$ systems were immediately sealed in an aluminum pan for characterization by the NETZSCH DSC 200 F3 instrument.

Acknowledgements

This work was financially supported by the National Basic Research Program of China (No. 2009CB939900), National Natural Science Foundation of China (No. 20801051, 20621061), and a China Postdoctoral Science Foundation funded project (20080430102).

[1] D. Balachandran, D. Morgan, G. Ceder, A. van de Walle, *J. Solid State Chem.* **2003**, *173*, 462.
[2] A. H. Heuer, A. Q. He, P. J. Hughes, F. H. Feddrix in *IBA-2000 Manganese Oxide Symposium, Argonne National Laboratory*, Chicago, IL, **2000**.
[3] P. M. De Wolff, *Acta Crystallogr.* **1959**, *12*, 341.
[4] Y. Chabre, J. Pannetier, *Prog. Solid. State. Chem.* **1995**, *1*, 23.
[5] D. E. Simon, T. N. Anderson, C. D. Elliott in *IBA-2000 Manganese Oxide Symposium, Argonne National Laboratory*, Chicago, IL, **2000**.
[6] a) D. Shechtman, I. Blech, D. Gratias, J. W. Cahn, *Phys. Rev. Lett.* **1984**, *53*, 1951; b) L. Bendersky, *Phys. Rev. Lett.* **1985**, *55*, 1461.
[7] S. Turner, P. R. Buseck, *Nature* **1983**, *304*, 143.
[8] a) J. Yang, C. Xue, S. H. Yu, J. H. Zeng, Y. T. Qian, *Angew. Chem.* **2002**, *114*, 4891; *Angew. Chem. Int. Ed.* **2002**, *41*, 4697; b) B. Mayers, Y. Xia, *Adv. Mater.* **2002**, *14*, 279; c) J. Polleux, N. Pinnna, M. Antonietti, M. Niederberger, *Adv. Mater.* **2004**, *16*, 436; d) Y. P. Fang, A. W. Xu, L. P. Xu, L. P. You, R. Q. Song, J. C. Yu, H. X. Zhang, Q. Li, H. Q. Liu, *Adv. Funct. Mater.* **2003**, *13*, **955**.
[9] a) F. Y. Cheng, J. X. Chen, L. Gou, P. W. Shen, *Adv. Mater.* **2005**, *17*, 2753; b) X. Wang, Y. D. Li, *Chem. Eur. J.* **2002**, *9*, 300.
[10] Y. J. Xiong, Y. Xie, Z. Q. Li, C. Z. Wu, *Chem. Eur. J.* **2003**, *9*, 1645.
[11] C. Z. Wu, Y. Xie, D. Wang, J. Yang, T. W. Li, *J. Phys. Chem. B* **2003**, *107*, 13583.
[12] W. N. Li, J. K. Yuan, X. F. Shen, S. Gomez-Mower, L. P. Xu, S. Sithambaram, M. Aindow, S. L. Suib, *Adv. Funct. Mater.* **2006**, *16*, 1247.
[13] L. X. Yang, Y. J. Zhu, W. W. Wang, H. Tong, M. L. Ruan, *J. Phys. Chem. B* **2006**, *110*, 6609.
[14] J. K. Yuan, K. Laubernds, Q. H. Zhang, S. L. Suib, *J. Am. Chem. Soc.* **2003**, *125*, 4966.
[15] C. Poinsignon, E. Djurado, H. Klein, P. Strobel, F. Thomas, *Electrochim. Acta* **2006**, *51*, 3076.
[16] Y. S. Ding, X. F. Shen, S. Gomez, H. Luo, M. Aindow, S. L. Suib, *Adv. Funct. Mater.* **2006**, *16*, 549.
[17] L. I. Hill, A. Vervaere, *J. Solid State Chem.* **2004**, *177*, 4706.
[18] F. Y. Cheng, J. Z. Zhao, W. Song, C. S. Li, H. Ma, J. Chen, P. W. Shen, *Inorg. Chem.* **2006**, *45*, 2038.
[19] a) C. D. Wanger, W. M. Riggs, L. E. Davis, J. F. Moulder, G. E. Muilenberg, *Handbook of X-ray Photoelectron Spectroscopy*, Perkin–Elmer, Eden Prairie, **1978**; b) V. Subramanian, H. W. Zhu, R. Vajtai, P. M. Ajayan, B. Q. Wei, *J. Phys. Chem. B* **2005**, *109*, 20207.
[20] Y. Chabre, J. Pannetier, *Prog. Solid State Chem.* **1995**, *23*, 1.
[21] J. E. Post, *Natl. Proc. Acad. Sci. USA* **1999**, *96*, 3447.
[22] A. M. Byström, *Acta Chem. Scand.* **1949**, *3*, 163.
[23] a) G. C. Xi, Y. Y. Peng, Y. C. Zhu, L. Q. Qiang, W. Q. Zhang, W. C. Yu, Y. T. Qian, *Mater. Res. Bull.* **2004**, *39*, 1641–1648; b) X. Wang, Y. D. Li, *Chem. Eur. J.* **2003**, *9*, 300; c) G. L. Wang, B. Tang, L. H. Zhuo, J. C. Ge, M. Xue, *Eur. J. Inorg. Chem.* **2006**, 2313.
[24] D. E. Simon, R. W. Morton, J. J. Gislason, *Adv. X-ray Anal.* **2004**, *47*, 267.
[25] a) Y. Chen, L. S. Yang, C. Feng, L. P. Wen, *Biochem. Biophys. Res. Commun.* **2005**, *337*, 52; b) S. T. Stern, S. E. McNeil, *Toxicol. Sci.* **2009**, *101*, 4; c) G. Lv, F. He, X. M. Wang, F. Gao, G. Zhang, T. Wang, H. Jiang, C. H. Wu, D. D. Guo, X. M. Li, B. A. Chen, Z. Z. Gu, *Langmuir* **2008**, *24*, 2151.
[26] a) B. E. Zalba, M. M. Je, L. F. Cabeza, *Appl. Therm. Eng.* **2003**, *23*, 251; b) M. N. A. Hawlader, M. S. Uddin, M. M. Khin, *Appl. Energy* **2003**, *74*, 195.
[27] a) T. P. Leervad Pedersen, J. Kalb, W. K. Njoroge, D. Wamwangi, M. F. Spaepen Wuttig, *Appl. Phys. Lett.* **2001**, *79*, 3597; b) J. A. Kalb, C. Y. Wen, F. Spaepen, H. Dieker, M. Wuttig, *J. Appl. Phys.* **2005**, *98*, 054902.
[28] a) K. Lu, Y. Li, *Phys. Rev. Lett.* **1998**, *80*, 4474; b) J. F. Huang, L. S. Bartell, *J. Phys. Chem.* **1995**, *99*, 3924.

Received: September 3, 2008
Published online: November 25, 2008

